Remote Sensing of Environment 304 (2024) 114074

Contents lists available at ScienceDirect

Remote Sensing of Environment

journal homepage: www.elsevier.com/locate/rse

Mapping icebergs in sea ice: An analysis of seasonal SAR backscatter at C- and L-band

Laust Færch [a,*], Wolfgang Dierking [a,b], Nick Hughes [c], Anthony P. Doulgeris [a]

[a] Center for Integrated Remote Sensing and Forecasting for Arctic Operations, Department of Physics and Technology, UiT—The Arctic University of Norway, 9019 Tromsø, Norway
[b] Alfred Wegener Institute, Helmholtz Center for Polar and Marine Research, Germany
[c] Norwegian Meteorological Institute, Norway

ARTICLE INFO

Edited by Menghua Wang

Keywords:
Arctic
Belgica Bank
SAR
Icebergs
Sea ice

ABSTRACT

Icebergs in the Arctic can pose a threat to maritime traffic and offshore installations and influence the properties of the upper ocean layer. While icebergs in open water are regularly monitored using C-band SAR satellites, less attention has been paid to icebergs in regions with a high areal fraction of sea ice, where detection using traditional methods is more difficult. In this study, we compare the capability of C- and L-band SAR to detect icebergs in level and deformed fast sea ice across various seasons. To this end we use a timeseries of SAR images acquired at HH- and HV-polarization in 2019 and 2020, covering respectively 301 and 356 icebergs. As reference data for validation, we used iceberg polygons derived from Sentinel-2 images. Our results reveal that compared to C-band, L-band SAR is significantly better at separating the backscatter of icebergs and sea ice and thus is preferable for detecting icebergs in ocean regions with a high sea ice concentration. It is further shown that L-band SAR is less affected by melting conditions, suggesting that it can be used for iceberg detections in both summer and winter.

1. Introduction

The calving of icebergs is one of the main sources of mass loss from ice sheets and glaciers. For the Greenland ice sheet, it is estimated that the annual solid ice discharge is on the order of 500 Gt/year (Mankoff et al., 2020). A large fraction of this discharge takes the form of medium and large icebergs (60–220 m in length), that float out into the ocean.

Icebergs act as large freshwater reservoirs to the ocean, and melting icebergs are therefore a direct source of freshwater to the ocean, leading to a reduction of salinity and cooling of the local water column, which affects ocean circulation and facilitates the formation of sea ice (Bügelmayer et al., 2015; Marson et al., 2021). This is especially significant in areas with a high iceberg density (Bigg, 2015, Ch. 4). Icebergs also pose a major threat to maritime traffic and offshore installations in the Arctic. Detecting and mapping the location of icebergs are therefore important both for ocean models and for maritime safety.

Typically, icebergs in open water can be detected using Synthetic Aperture Radar (SAR) satellites, and this is regularly done with C-band satellites such as Sentinel-1 or RADARSAT (Gill, 2001; Power et al., 2001; Sandven et al., 2007). Normally, iceberg detection algorithms are based on the observation that icebergs exhibit higher backscatter than the surrounding open water (Willis et al., 1996), and thus appear as bright spots against the darker ocean in SAR images. This can be utilized to find clusters of pixels with a high contrast relative to the local background, e.g., using a statistical approach such as the Constant False Alarm Rate (CFAR) detector (Oliver and Quegan, 2004). CFAR detectors have been used to map regional distributions of icebergs in open water in the Arctic, e.g., in Buus-Hinkler et al. (2014), and are currently being used to create operational iceberg density products by the Copernicus Marine Service for the waters around Greenland, Labrador and Newfoundland (Copernicus Marine Service, 2023).

However, mapping icebergs in regions with sea ice is more difficult using these techniques. This is mainly because sea ice exhibits highly variable backscatter, making it more difficult to detect outliers of backscattered intensity which can be related to icebergs (Dierking, 2020). This is especially difficult for rough or deformed sea ice, which is well known to have a higher and more variable backscatter response than level ice, thus lowering the contrast between icebergs and their background (Wesche and Dierking, 2012). Further, the backscatter response of sea ice shows seasonal variations (Haas, 2001), due to the

* Corresponding author.
E-mail address: laust.farch@uit.no (L. Færch).

https://doi.org/10.1016/j.rse.2024.114074
Received 23 August 2023; Received in revised form 16 February 2024; Accepted 19 February 2024
Available online 24 February 2024

related temperature changes (Casey et al., 2016; Yackel et al., 2007), that must be considered in algorithms for detecting icebergs in sea ice. In particular, melting is known to have a large impact on iceberg backscatter (Willis et al., 1996; Ferdous et al., 2019). Thus, icebergs in sea ice and close to the ice margin are currently not included in operational monitoring products, and a recent survey by the International Ice Charting Working Group (IICWG) noted that icebergs in sea ice should be considered in future operational ice charting products (IICWG, 2019).

The radar response of icebergs and sea ice arises primarily from a combination of surface and volume scattering (Willis et al., 1996; Haas, 2001; Power et al., 2001; Wesche and Dierking, 2012), where the exact contribution of each component is heavily influenced by the presence of water or wet snow on the surface and the salinity of the ice. Under freezing (dry) conditions and at low salinity, radar signals typically penetrate deeper into snow and ice than under thawing (wet) conditions and high salinity. Thus, the ability to distinguish between icebergs and sea ice in SAR images depends on both meteorological conditions and on the type of the surrounding sea ice (Mazur et al., 2017).

Even though some studies have suggested methods to detect icebergs in sea ice using C-band SAR, e.g., in Marino et al. (2016) and Zakharov et al. (2017), these studies did not consider the seasonal aspects or the influence of different types of sea ice. Other studies focusing on the Antarctic, typically employ object- or segmentation-based methods (Kim et al., 2011; Mazur et al., 2017; Barbat et al., 2019; Koo et al., 2023; Evans et al., 2023; Braakmann-Folgmann et al., 2023), which are not suitable for the Arctic where the smaller icebergs often only cover a few pixels in the SAR image. For the Arctic, studies covering larger regions with different ice types, e.g., by Dierking and Wesche (2014), and Soldal et al. (2019) reported difficulties to reliably detecting icebergs because of a large overlap in the backscatter characteristics of icebergs and sea ice.

It is expected that L-band SAR might improve iceberg detection in sea ice considering the longer wavelength and hence larger penetration depth into wet snow and ice and lower sensitivity to small-scale surface roughness (Casey et al., 2016; Rignot et al., 2014; Dierking and Davidson, 2020). This is quite interesting considering that several recent and planned launches of L-band SAR satellites, such as SAOCOM (Giraldez, 2004), NISAR (Das et al., 2021), and ROSE-L (Davidson et al., 2021), will increase the amount of available L-band data for the Arctic in the future.

However, only a few studies of iceberg detection using L-band SAR images have been carried out to date, e.g., by Marino (2018) and Bailey et al. (2021). And direct comparisons of C- and L-band SAR data for detecting icebergs in sea ice have not been attempted before. Given how radar signatures are affected by different meteorological and sea ice conditions, studies considering different sea ice types and covering different seasons are of high interest. Further, since small variations in iceberg geometry and orientation can affect backscatter responses significantly (Ferdous et al., 2018), studies must preferably be carried out using large datasets to avoid skewing the results. The validation of detection algorithms using a large independently obtained dataset covering different ice types and seasons has to our knowledge never been attempted due to the difficulties in obtaining the necessary data.

This study compares the backscatter contrast between icebergs and sea ice in C- and L-band SAR images, under different seasonal conditions. The contrast is used as an indicator for detectability, with high backscatter contrast between iceberg and sea ice indicating high detectability. The study is carried out using a large number of icebergs that are embedded in land-fast ice and a time series of SAR images covering several months, from freezing temperatures in the spring to the melting season later in the summer. Data from two separate years (2019 and 2020) were used in the study. The land-fast ice is segmented into regions of ice classified as either *level* or *deformed* to consider conditions in two main classes of sea ice. Although our results are technically restricted to icebergs in land-fast ice, we expect that our conclusions can be extended to icebergs in high-concentration drift ice of similar sea ice types. Additionally, large areas of the Arctic are covered in seasonal or permanent fast ice (Mahoney, 2018), and many of these areas are near ice-calving glaciers and ice caps (Wolken et al., 2020).

In summary our study helps to determine the limitations and advantages of using C- and L-band SAR, respectively, for mapping icebergs in areas with a high concentration of sea ice, especially considering different sea ice, and seasonal conditions.

2. Study area and data

2.1. Study area

The study was carried out over an area of interest (AOI) covering a section of Belgica Bank in north-eastern Greenland located between 78 and 80°N and 12–16°W. Our AOI covers approximately 23.000 km^2 in total. West of the AOI, two large ocean-terminating glaciers are located, the Nioghalvfjerdsbræ, and the Zachariae Isstrøm, each calving several gigatons of solid ice each year (Mankoff, 2020). East of the AOI, the East Greenland Current (EGC) transports large amounts of sea ice from the Arctic into the North Atlantic (Hughes et al., 2011).

A large area of Belgica Bank is shallow with depths <100 m, while it is surrounded by deep troughs of 300–400 m depth (Arndt, 2015). Many of the icebergs that calved from the glaciers ground on the shallow bank. Here, they are surrounded by sea ice transported down from the Arctic Ocean with the EGC. The icebergs block and catch some of the sea ice floes, and when the fast ice starts forming from the coast to the bank, the sea ice floes are embedded within the fast ice (Hughes 2011). This means that our AOI covers a large number of icebergs of varying sizes between 30 to 40 m and larger than a kilometer, and many different types of sea ice. Towards the open water on the eastern side of the bank, the land fast ice tends to be rough or deformed, consisting of the older floes from the north, while on the western side, the sea ice is typically newly formed and less deformed (level sea ice). Since both the sea ice and icebergs remain stationary for a long period, from winter freeze to summer melt, this is one of the best places in the Arctic to investigate how the backscatter response from icebergs and sea ice develops over different seasons.

2.2. Remote sensing data

L-band SAR images are from the ALOS-2 satellite, and C-band images from Sentinel-1. A time series of ALOS-2/PALSAR-2 images was provided by JAXA. It was acquired in ScanSAR Nominal, right-looking mode on a descending orbit (Fig. 1) and was delivered in a georeferenced Level 1.5 GeoTIFF format, however without incidence angle information.

Sentinel-1 images are available from the Copernicus program through an open data policy, and therefore it is possible to get almost daily coverage for our AOI with Sentinel-1. However, since our main interest is a comparison between C- and L-band, we opted to only download Sentinel-1 images from days when an ALOS-2 image was acquired. For a few of the ALOS-2 images, no image was available from Sentinel-1 from the same day. In these cases, the image nearest in time was used instead, which was typically an acquisition from the following or previous day. However, for most of the ALOS-2 images, a Sentinel-1 acquisition could be found within a time difference of 6 h.

The Sentinel-1 images were acquired in Extra Wide-Swath (EW) mode and were retrieved from the CREOtech Data and Information Access Service (CREODIAS) and processed using the Sentinel Applications Platforms (SNAP), including thermal noise removal, calibration, and ellipsoid correction. All Sentinel-1 acquisitions were acquired in a right-looking geometry and from descending orbits.

Referring to Fig. 1, since all images from both Sentinel-1 and ALOS-2 were acquired in right-looking geometries and from descending orbits, the near-range is on the right side of the images, and the far range on the left side. Both the C- and L-band images are acquired in dual-

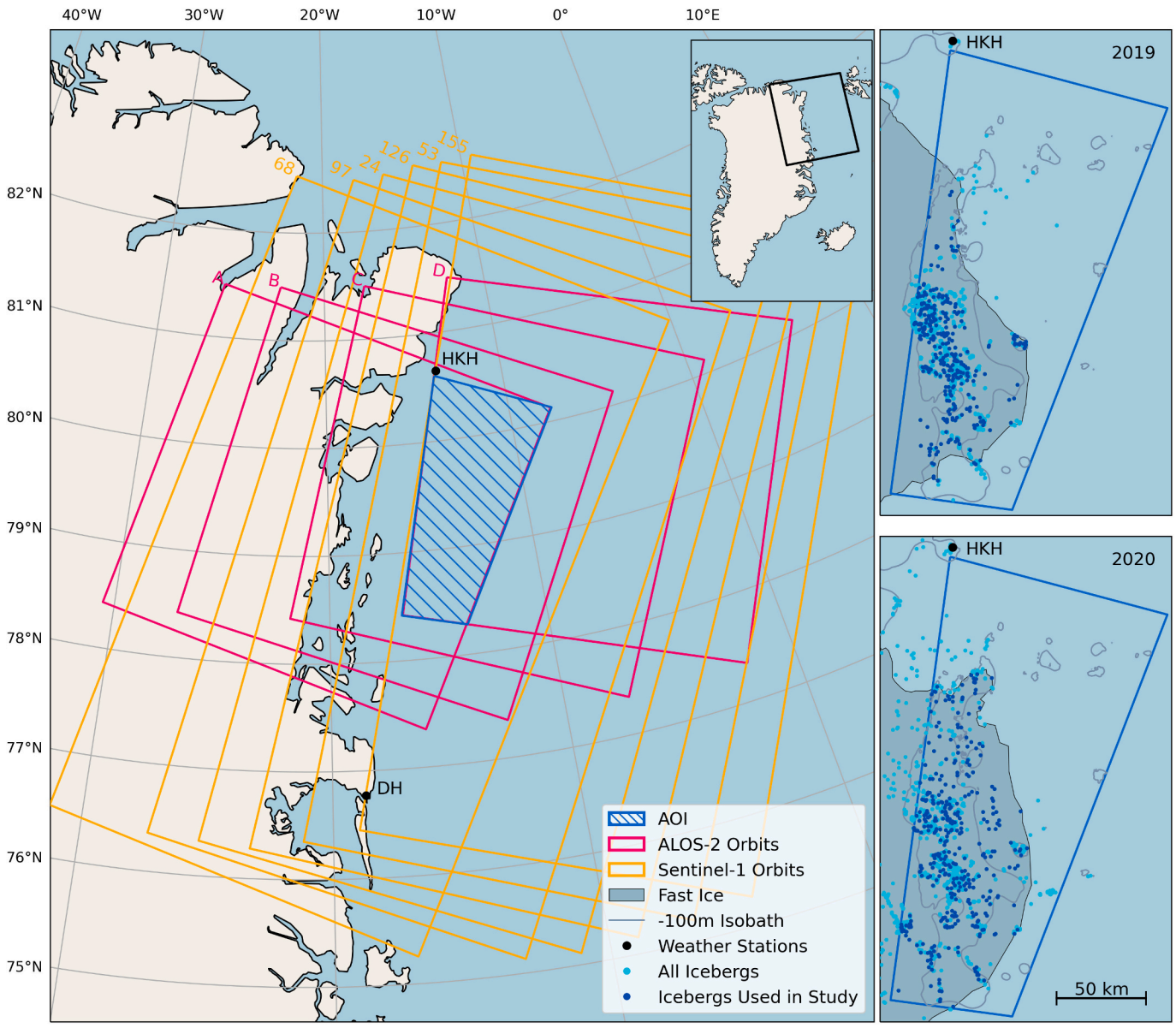

Fig. 1. Overview of the study area showing the AOI and the orbits from Sentinel-1 (orange) and ALOS-2 (red). The black dots mark the weather stations at Henrik Krøyer Holme (HKH), and Danmarkshavn (DH) respectively. On the right, the icebergs from 2019 and 2020 are shown, together with the fast-ice edge in mid-July, and the −100-m isobath from IBCAO V4.1 (Jakobsson et al., 2020). (For interpretation of the references to colour in this figure legend, the reader is referred to the web version of this article.)

polarization (HH, HV) mode, which is commonly used for sea ice mapping in the Arctic (Dierking, 2020) and hence widely available for iceberg detection in the Arctic as well.

A total of 22 ALOS-2 images were used from 2019 and 19 images from 2020, complemented by 14 Sentinel-1 images for 2019, and 17 images for 2020. All images were acquired in the period between April 1st and August 1st, covering the freezing season in the spring until the fast ice break up during summer. An overview of the image characteristics can be found in Table 1.

To complement the SAR data and for generating a validation data set, optical images from the European Sentinel-2 satellites were downloaded from CREODIAS. Here we used the RGB bands (B4, B3, and B2) at 10-m resolution.

Table 1
Overview of the SAR data used in the study. The Noise Equivalent Sigma Zero (NESZ)of Sentinel-1 varies with the incidence angle. *For ALOS-2, the NESZ is given in the mission requirements, but the actual value may be lower.

	Mode	NESZ*	Pixel Spacing	Looks (range, azimuth)	Polarization	Swath Width	Incidence Angle
Sentinel-1[a]	Extra Wide Swath (EW)	−24: −34 db	40 m	6 × 2	HH, HV	410 km	18.9–40.0
ALOS-2[b,c]	ScanSAR mode (WBD)	−26 db	25 m	2 × 3	HH, HV	360 km	22.7–45.9

[a] Bourbigot et al. (2016).
[b] JAXA (2012).
[c] Kankaku et al. (2013).

2.3. Validation data

Iceberg polygons served as validation data for the study. The polygons were drawn manually using optical Sentinel-2 images by experts from the Norwegian Meteorological Institute (MET Norway) (Amdal and Hughes, 2022). The icebergs are easily distinguishable in the optical images acquired in the spring when the sun is illuminating the icebergs from a very small grazing angle, thus generating distinct shadows.

To account for small errors in the geocoding, Sentinel-2 iceberg polygons shorter than 100 m in length were not considered in the analysis of the SAR images. Here, the length is calculated as the major axis of the minimum bounding rectangle of the iceberg polygon. Furthermore, icebergs that were within 400 m of a neighboring iceberg were also removed from the dataset to avoid mixing signals from several icebergs forming a cluster (see Section 3.3). Icebergs outside the AOI and the fast-ice edge were not considered in our analysis. Since the fast ice edge is slowly changing during the season, we used the fast ice edge from mid-July (see Fig. 1). That way, we ensure that all icebergs used for validation remain stationary for the entire study period. In total, 301 icebergs for 2019 and 356 icebergs for 2020 were used in the study. Examples of the different types of data used in the study are shown in Fig. 2.

2.4. Meteorological data

Temperature data from two weather stations close to the AOI were

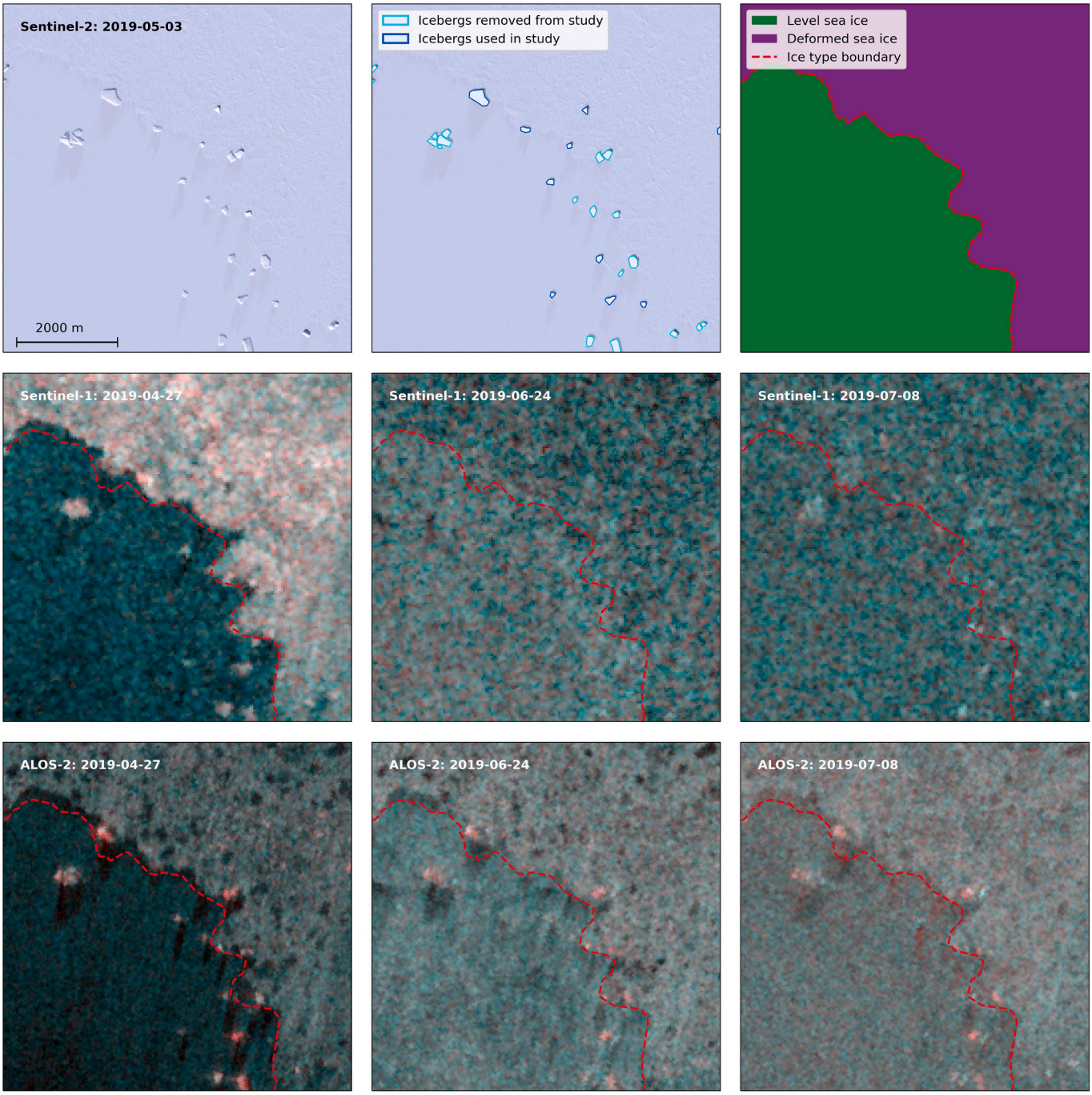

Fig. 2. Examples of the data used for the study. All images are covering the same subset of the AOI. The SAR images are colored as red: HV, green: HH, blue: HH. (For interpretation of the references to colour in this figure legend, the reader is referred to the web version of this article.)

downloaded from the Danish Meteorological Institute (Danish Meteorological Institute, 2023). The positions of the two stations are marked in Fig. 1. The southern part of the AOI has a higher iceberg density, which compensates for the larger distance of the southern weather station. Therefore, the overall temperature profile for our AOI was calculated as a daily average between the data from the two stations.

3. Methods

3.1. Method outline

As mentioned in Section 1, the main goal of this study is to compare the capability of C- and L-band SAR for detecting icebergs in level and rough sea ice under different seasonal conditions. To achieve this goal, we used the backscatter contrasts at HH- and HV-polarization between icebergs and the surrounding sea ice as a proxy for detectability. Therefore, we extracted the backscatter values for icebergs and sea ice and calculated the contrast for the entire timeseries (Sect. 3.3). Since we have to distinguish between level and deformed sea ice, a segmentation of the two types within our AOI was performed first (Sect. 3.2). A peculiarity of the radar response at L-band is the occurrence of time-delayed reflections which we discuss in Sect. 3.4.

In subsequent analyses presented in section 4 we explored whether the seasonal pattern of the backscattering contrast between icebergs and sea ice reveals any distinct seasonal patterns due to temperature variations, which is the case for sea ice backscatter (Haas, 2001; Casey et al., 2016; Yackel et al., 2007). Based on this analysis, the data were separated into freezing and melting periods. For each period, we investigated the variations of the backscattering coefficients from icebergs and sea ice for both C- and L-band to determine overlaps between the classes. This part of the study will also help to define boundaries in the backscatter at HH- and HV-polarization that might be useful for separating iceberg and sea ice signatures and improve existing detection algorithms.

3.2. Segmentation of level and deformed sea ice

A semi-automatic method was used to segment the fast ice into regions containing predominantly level and deformed sea ice. The segmentation was based on the observation that deformed ice generally exhibits higher backscatter values than level ice at both C- and L-band during winter (Dierking, 2010; Guo et al., 2022). Because we focus on fast ice, high backscattering, e.g., from pancake or brash ice or from frost-flower covered young ice in refreezing leads, can be excluded. Since the distribution of deformed and level ice does not change within the fast ice in the AOI, segmentation could be performed on images acquired before melt. For both 2019 and 2020, a single Sentinel-1 and a single ALOS-2 image were chosen for the segmentation. The images were manually selected based on appearance, showing strong visual distinction between level and deformed sea ice. The Sentinel-1 images were acquired on 2019-04-27 and 2020-04-09, and the ALOS-2 images on 2019-05-12 and 2020-04-26.

For each of the years, the two images were then stacked into a single image containing four bands (HH- and HV-polarization for both C- and L-band) and then processed by applying a Simple Linear Iterative Clustering (SLIC) segmentation algorithm (Achanta et al., 2012) using the scikit-image library (van der Walt et al., 2014) in Python. The SLIC algorithm uses a K-means approach to generate super-pixels, i.e., regions with high statistical similarity of the backscatter in the image. The SLIC algorithm used here was initialized with 1000 segments and a pre-processing Gaussian kernel of width 4 to reduce the speckle noise. Before applying the SLIC algorithm, each band of the image was truncated to the 5 and 95 quantiles decibel values, and then scaled to values between 0 and 1.

The resulting super-pixel polygons from the segmentation algorithm were then manually classified as either level or deformed sea ice. This was done by looking at the average backscatter levels within each segment and marking low-backscatter segments as *level* and high-backscatter segments as *deformed*. This manual classification was aided by optical Sentinel-2 images where in doubt. The area outside the mid-July fast-ice edge was marked as drift ice and thus not used in the study. This approach greatly eased the process of classification compared to drawing all the polygons by hand.

The resulting classified images are shown in Fig. 3. For 2019, 124 icebergs were located in level ice and 177 in deformed ice. For 2020, only 43 icebergs were found in level ice (because of a lower areal fraction of this ice type), and 313 in deformed ice.

3.3. Time-delayed reflections

A peculiarity that was observed in the ALOS-2 images was that the main backscatter return of the icebergs did not appear at the exact location of the iceberg polygons derived from the Sentinel-2 images. Rather the main reflection from the icebergs typically appeared some hundreds of meters down-range from the polygons. This shift is not caused by bad geolocation of the ALOS-2 images since the land and sea-ice boundaries are placed at the correct location, as seen in the optical images. The phenomenon was also observed in high-resolution ALOS-2 Stripmap images of the AOI (Fig. 4, top right) and have previously been observed for icebergs in open water as well (Færch et al., 2023).

Gray and Arsenault (1991) reported that icebergs could cause time-delayed reflections when imaged with L-band SAR. This was caused by the lower attenuation loss of the L-band signal in ice compared to the C-band signal, which means that radar signals penetrate the iceberg completely and are reflected from the bottom and the side walls. This means that from an L-band SAR perspective, the main and strongest reflection does not appear at the true location of the iceberg but rather a few hundred meters down range, due to the longer traveling path of the radar signal through the iceberg. Therefore, we extracted the backscatter values from the main reflection down-range which requires to consider the time delay of the signal, i.e., the spatial shift between the true location of an iceberg (from the Sentinel-2 imagery) and the backscatter maximum in the ALOS-2 image.

An exact calculation of the time delay of a single iceberg as a function of radar incidence angle is not possible, since it depends in addition on the sometimes very complex iceberg geometry (shape, height, length, width), the effective dielectric constant, the properties of potentially present snow and firn layers on the iceberg surface and any saline ice layers frozen to the iceberg.

The height of the icebergs could be inferred from the bathymetry assuming that they are all grounded. However, this assumption might not always hold for small icebergs that have broken off from larger bergs just before the consolidation of the land-fast ice. Additionally, the bathymetry data for the area also have uncertainties due to the sparse sampling in this region (Arndt et al., 2015), which necessarily adds uncertainty to the dataset.

In addition, the radar signal path in the iceberg may be variable as discussed in Gray and Arsenault (1991) and in Dierking and Wesche (2014). As multiple reflections within the iceberg (e.g., between bottom, side walls, and surface) may increase the time-delay and cause a more complex backscattering response of the iceberg, which again depends on the internal geometry of the icebergs.

Therefore, we developed a simple automatic matching method to identify the main backscatter reflection from each iceberg based on the observed backscatter intensities. This was done by iteratively shifting the iceberg polygons down-range in steps of 25 m, starting from 0 m and with a maximum distance of 350 m. Since a majority of the measured time delays were in the order of 50–200 m, a maximum distance of 350 m was chosen as an appropriate upper boundary. For each step, the average HV backscatter was calculated, and the original polygon was moved to a new location corresponding with the maximum backscatter within the (see Fig. 4). The HV backscatter was used here since it was

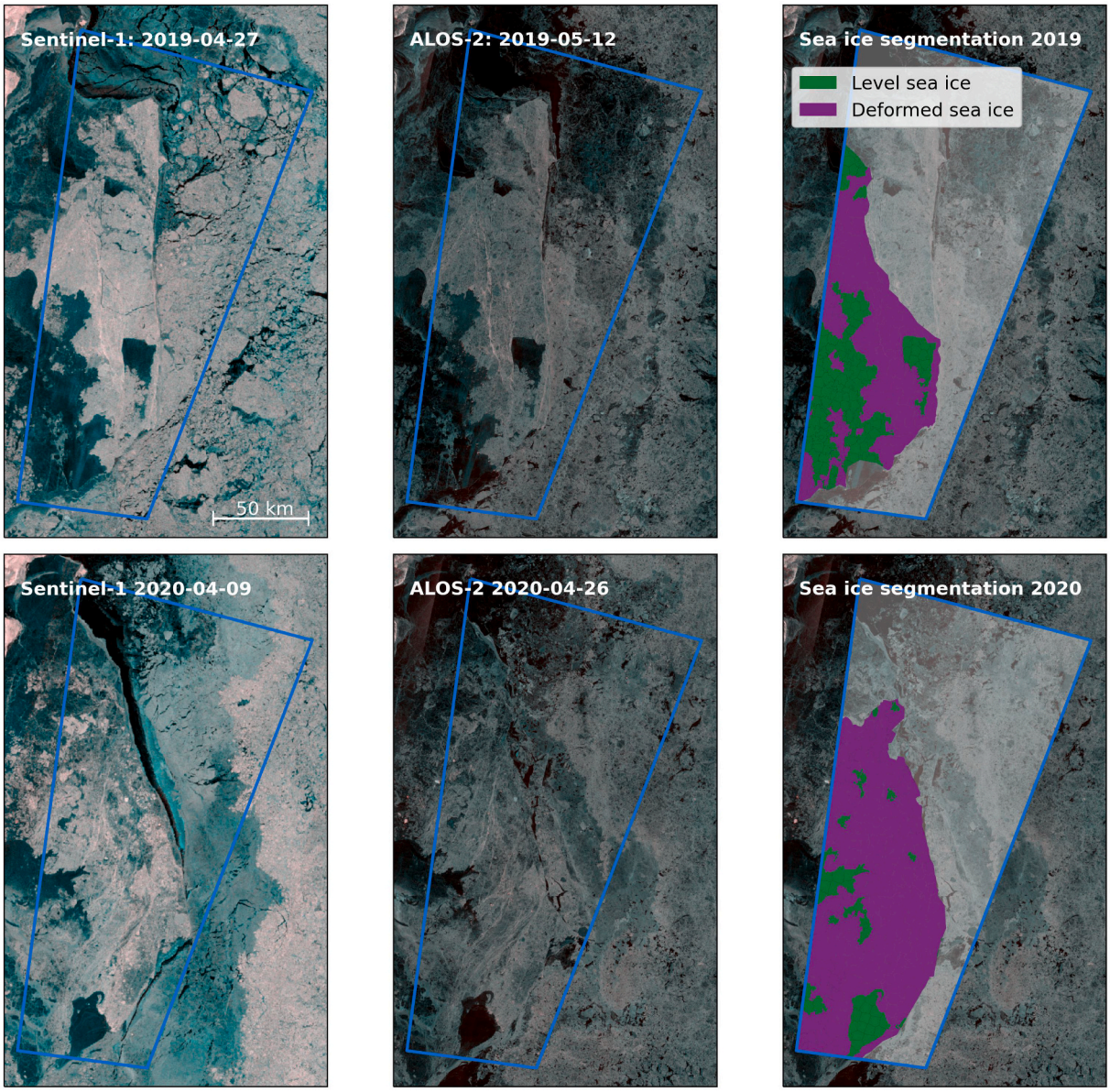

Fig. 3. Sea ice segmentation for 2019 (top) and 2020 (bottom) using the Sentinel-1 (left) and ALOS-2 images (center). The segmentation results (right) show level sea ice (green), deformed sea ice (purple), and drift ice (transparent gray). The AOI is marked with a blue polygon. The SAR images are colored as red: HV, green: HH, blue: HH. (For interpretation of the references to colour in this figure legend, the reader is referred to the web version of this article.)

observed that the contrast between icebergs and sea ice is significantly higher in the HV band compared to the HH band, this is e.g., seen in Figs. 2 and 4 where the icebergs in L-band is clearly distinguishable by their red colour. This may be explained by a recent study which reports that cold icebergs at L-band show a predominance of volume scattering (Bailey and Marino, 2020).

All time delays determined as described above were in the range between 0 and 300 m. In order to avoid mixing signals of neighboring icebergs, all icebergs with neighbors closer than 400 m were discarded from the analysis as described in Section 2.3. The process was repeated for all icebergs in all ALOS-2 images, as different orbits and meteorological conditions are also expected to affect the penetration and thus time delay.

3.4. Extraction of backscatter and contrast values

All icebergs in the dataset were classified according to the predominant sea ice type in which they were embedded (level or deformed), using the results from the segmentation in Section 3.2. Then, for each iceberg, a single backscatter value was extracted using the iceberg polygon. This was done by calculating the average backscatter (in linear intensity) of all the pixels that were touched by the polygon. The number of pixels used for calculating this average backscatter thus varies according to the size of the iceberg.

The backscatter of the surrounding sea ice (background) was also extracted for each iceberg. This was done using a window of 1600 × 1600 meters centered around the iceberg. Here, the iceberg polygons were used to mask out icebergs from the background to avoid contaminating the background backscatter with iceberg samples. In addition, if the icebergs were located close to an edge between different sea ice classes, the smallest class was also masked to avoid contamination. As such, the number of pixels used to estimate the background backscatter levels also varies depending on iceberg size, location of nearby icebergs, and variations of sea ice deformation. But generally, the average background backscatter is estimated using a larger number of pixels than the iceberg backscatter. As above, the calculation of the average sea ice

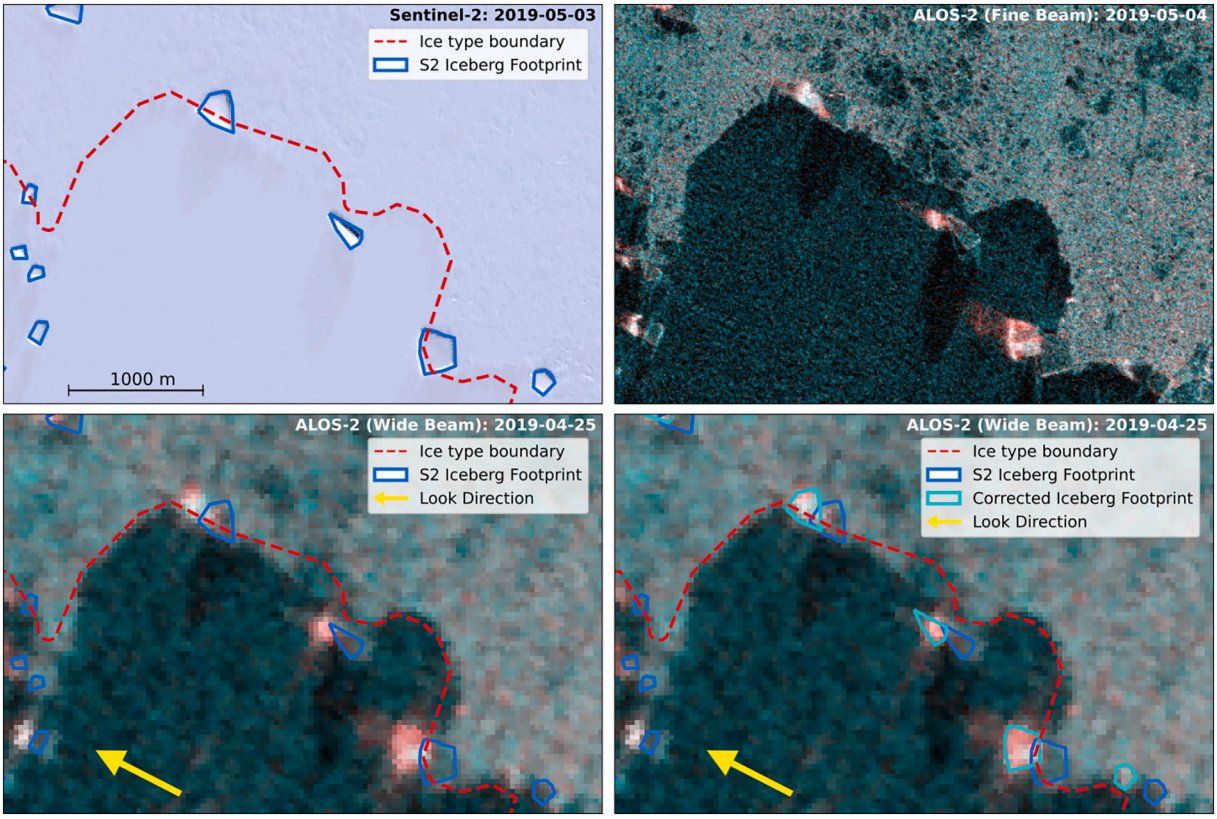

Fig. 4. Time-delayed reflection in L-band SAR images. The main reflection in the SAR image does not correspond with the location of the iceberg polygons from Sentinel-2 (blue outline). The edge between level and deformed sea ice in the SAR image, however, matches the boundary from the optical image (red dotted line). An automatic matching algorithm finds the main reflection down-range (cyan outline), by shifting the polygons downrange (yellow arrow). The SAR images are colored as red: HV, green: HH, blue: HH. (For interpretation of the references to colour in this figure legend, the reader is referred to the web version of this article.)

backscatter was also performed in the linear intensity domain.

The extraction of the average intensities was done for each iceberg in each scene. For the ALOS-2 images, the iceberg polygons were corrected as described in Section 3.3. Then, the contrast was calculated for each iceberg as the ratio between the means of iceberg and sea ice backscatter. The results were then grouped according to several parameters such as sensor, acquisition date, satellite orbit, polarization, and sea ice type. The calculations were done using Python 3.10, with the Numpy (Harris et al., 2020), GeoPandas (Jordahl, 2014), and Rasterio (Gillies et al., 2013) libraries.

3.5. Automatic iceberg detection

In addition to an analysis of the backscatter, an automatic iceberg detection algorithm was tested on selected images to compare the detection rate for icebergs in level and deformed sea ice using C- and L-band images, respectively. For this purpose, a commonly used iceberg detection algorithm of CFAR type was applied to two Sentinel-1 and two ALOS-2 images respectively. For both sensors, we chose one image from 2019 and one image from 2020. The first Sentinel-1 and ALOS-2 images were acquired on April 27th, 2019, with the ALOS-2 image from orbit D and the Sentinel-1 image from orbit 126 (see Fig. 1). Also in 2020, both images were acquired on April 27th, from orbit B (ALOS-2), and orbit 126 (Sentinel-1). Hence, the algorithm could be tested on images covering two distinct ice conditions. Since the ALOS-2 and Sentinel-1 images are in different native resolution, the ALOS-2 images were resampled to the same pixel spacing as the Sentinel-1 images using nearest neighbor interpolation.

A Normalized Intensity Sum (NIS) detector was chosen to find outliers (Liu, 2015). When applied to dual-pol data, the NIS detector works by calculating a new channel as the sum of normalized intensities of the HH and HV channels. If we assume that the individual HH and HV channels follow a gamma distribution, then the NIS channel also follows a gamma distribution. As such, a gamma based CFAR detector can then be applied to the NIS channel to delineate outliers (Færch et al., 2023).

For the CFAR detector we used a probability of false alarm rate of 1e-14. Clutter estimation was carried out in a circular window with a diameter of 17 pixels, corresponding to 680 m at 40-m pixel spacing, and with a circular guard region with a diameter of 10 pixels, corresponding to 400 m. This means that the detector is optimized for icebergs smaller than 200 m in length, while it should also be able to detect slightly larger icebergs. The detection algorithm uses a fixed clutter region, i.e., it does not adapt to icebergs within the clutter estimation window, which means that the method is not optimal in areas with a high iceberg density due to the risk of iceberg pixels being included in the clutter estimation window.

Since the algorithm marks pixel outliers, groups of connected pixels were merged into polygons for further analysis. Here, polygons of a size of 3 pixels or smaller were discarded to avoid too many false positives caused by speckle. The computed polygons were then compared with the Sentinel-2 iceberg polygons. As mentioned earlier, icebergs smaller than 100 m in length were ignored, and icebergs outside the fast-ice edge were also removed from the analysis. To account for the time-delayed reflections at L-band, all detections from ALOS-2 were moved up-range by a fixed distance corresponding to the average time-delay for all the analysed icebergs. The distances were 100 m for the image acquired on 2019-04-27, and 160 m for the image from 2020 to 04-27. Icebergs in distances $\leq$400 m from other icebergs (i.e., icebergs in clusters) that were previously removed were kept in the validation data for this test. This procedure resulted in a total of 879 icebergs for 2019

(with 587 icebergs embedded in deformed sea ice, and 292 in level sea ice) and 909 icebergs for 2020 (767 in deformed sea ice and 142 in level sea ice).

The results were then divided into three categories. 1) If an iceberg identified in the Sentinel-2 reference data was overlapped by a polygon detected by the CFAR algorithm, the iceberg was marked as a true positive (TP). 2) If a Sentinel-2 iceberg polygon was not overlapped by a CFAR polygon, then the iceberg was marked as a false negative (FN). 3) CFAR polygons that did not overlap with a Sentinel-2 polygon were marked as false positives (FP). To further evaluate the performance, we also calculated the *precision* and *recall*,

$$Recall = \frac{TP}{TP + FN}$$

$$Precision = \frac{TP}{TP + FP}$$

As such, a low recall indicates a high number of false negatives compared to the number of true positives, while a low precision indicates a high number of false positives compared to the number of true positives.

Finally, the results were separated between level and deformed ice according to the outcome of the sea ice segmentation (Section 3.2), to distinguish the performance for icebergs in level and deformed sea ice.

4. Results

4.1. Backscatter contrast timeseries

In Figs. 5 and 6, the average backscatter contrasts between icebergs and their background are plotted for Sentinel-1 and ALOS-2 for each of the image acquisition dates. In the figures, we have also plotted the average daily temperature for the region. In addition, the different orbits used for each image have been marked to consider the influence of different incidence angles on the contrast. The backscatter contrast time series for Sentinel-1 are plotted in Figs. 5 for 2019 and 2020, respectively, while Fig. 6 show the ALOS-2 backscatter contrast time series for the two years, respectively.

The figures show that both Sentinel-1 and ALOS-2 offer a high contrast between icebergs and level sea ice during the beginning of each time series when temperatures are well below zero degrees Celsius, and that this contrast is higher for the HV polarization than for HH polarization. Additionally, we observe a decrease in the contrast when temperatures are close to or exceed 0 °C. For Sentinel-1, this decrease is clearly visible for level sea ice, while for ALOS-2, the decrease is visible for both sea ice types.

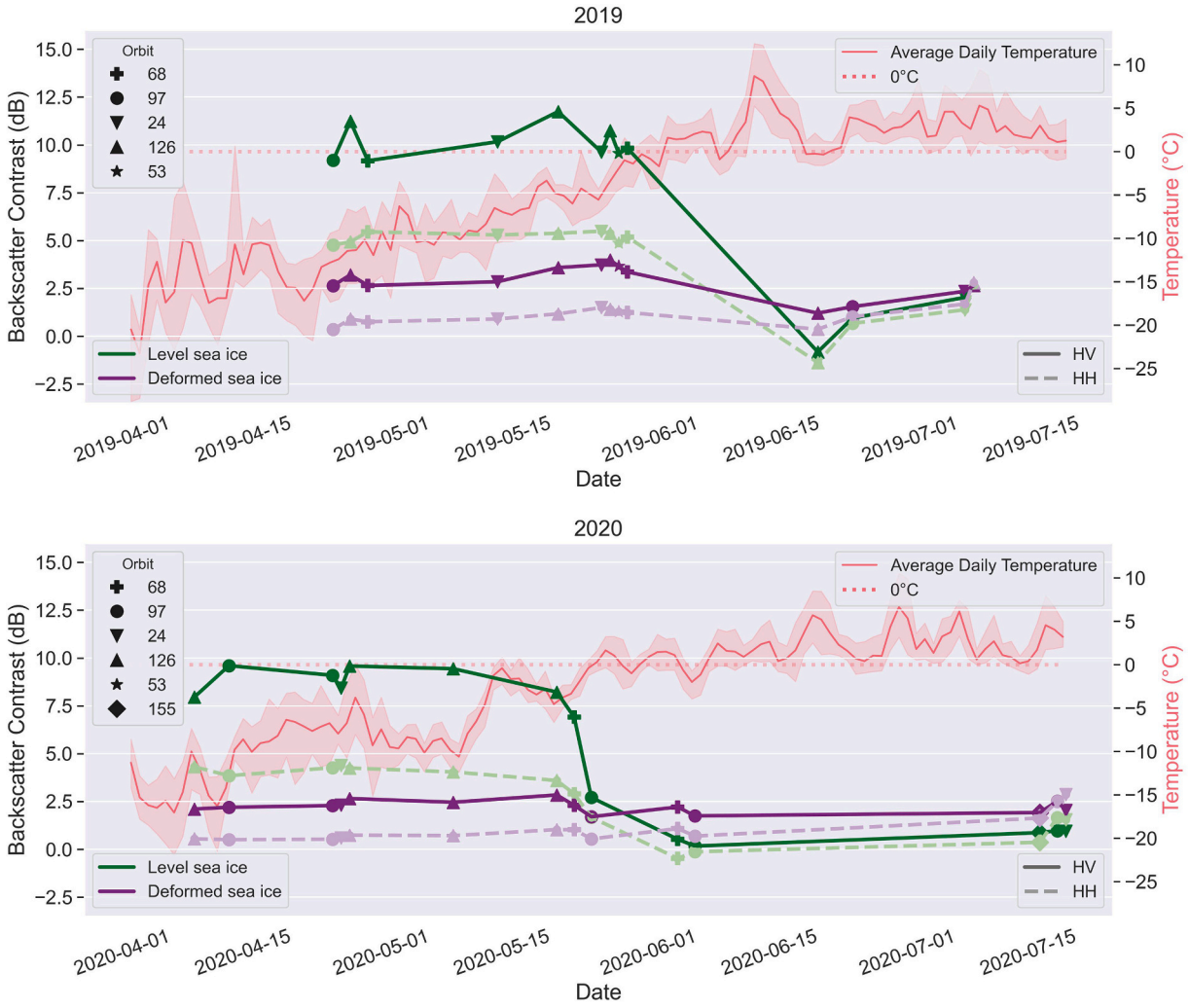

Fig. 5. Backscatter contrast for Sentinel-1 in 2019 (top) and 2020 (bottom). The contrast between level sea ice and icebergs (green) and deformed sea ice and icebergs (purple) are plotted for HV (full line) and HH (dashed line). The markers indicate the orbit numbers from Fig. 1. The daily temperature is plotted in the background (red), with shading indicating the fluctuations between daily minimum and maximum temperature. (For interpretation of the references to colour in this figure legend, the reader is referred to the web version of this article.)

Fig. 6. Backscatter contrast for ALOS-2 in 2019 (top) and 2020 (bottom). The contrast between level sea ice and icebergs (green) and deformed sea ice and icebergs (purple) are plotted for HV (full line) and HH (dashed line). The markers indicate the orbit numbers from Fig. 1. The daily temperature is plotted in the background (red), with shading indicating the fluctuations between daily minimum and maximum temperature. (For interpretation of the references to colour in this figure legend, the reader is referred to the web version of this article.)

Figure 5 reveals a high contrast for level sea ice throughout spring (8–12 dB for HV and 4–5 dB for HH). Around the onset of melt, the contrast is sharply decreasing down to 0 ±2 dB for both HV and HH. For deformed ice, the contrast is significantly lower during the spring, with values around 2–4 dB for HV and around 0–2 dB for HH. At the onset of melt, the contrast for deformed ice decreases slightly down to around 0–2 dB. There are large similarities between 2019 and 2020, although 2019 exhibits slightly higher contrast during the spring than 2020.

Comparing ALOS-2 (Fig. 5) to Sentinel-1 (Fig. 6), an overall higher contrast is recognized during spring for both level and deformed ice at both HH- and HV-polarization. For level ice, the contrast varies between 10 and 14 dB for HV, and 6–8 dB for HH, while for deformed sea ice it varies around 8–10 dB for HV and remains stable around 4 dB for HH. Like the contrast for Sentinel-1, the contrast for ALOS-2 also shows a sharp decrease after the onset of summer melt. However, where the contrast for Sentinel-1 during the thawing season decreases to around 0 ±2 dB, the ALOS-2 contrast remains higher, with magnitudes around 6 dB for level sea ice and 4–5 dB for deformed sea ice.

The ALOS-2 contrast plot shows a large variation during the spring, especially for level sea ice which varies around 11–16 dB for 2019, and 10–14 dB in 2020 for the HV polarization. This variation correlates with the orbit numbers, with orbit D showing the lowest contrast and orbit A showing the highest. Referring to the overview plot in Fig. 1, we note that orbit A corresponds to near-range in the image (low incidence angles), and D to far-range (high incidence angles). This suggests that the contrast for ALOS-2 is highly sensitive to the incidence angle, with low incidence angles offering better detectability of icebergs.

Based on the contrast plots, our dataset can be divided into two main categories as a function of the air temperature. We denote these conditions *freezing* and *thawing*, where *thawing* has been defined as starting at the first day on the year when the average temperature for the past five days exceeds 0°, which was on June 4th, 2019, and May 28th, 2020.

4.2. Seasonal scatterplots

To investigate the relationship between backscattered intensity from icebergs and the two main sea ice types more in detail, we have plotted the intensities for Sentinel-1 and ALOS-2 in Figs. 7 and 8, respectively. The plots highlight the distributions of the backscatter and the correlation between polarizations for the three classes. This is helpful for separating the various classes and selecting the optimum detectors for finding icebergs in areas with a high sea ice concentration. The results were separated into *freezing* and *thawing* seasons depending on the average temperature as described in Section 4.1. Fig. 7 shows the results for Sentinel-1 (C-band), with the top row containing data from 2019 and the bottom row for 2020. The left column shows the data under freezing

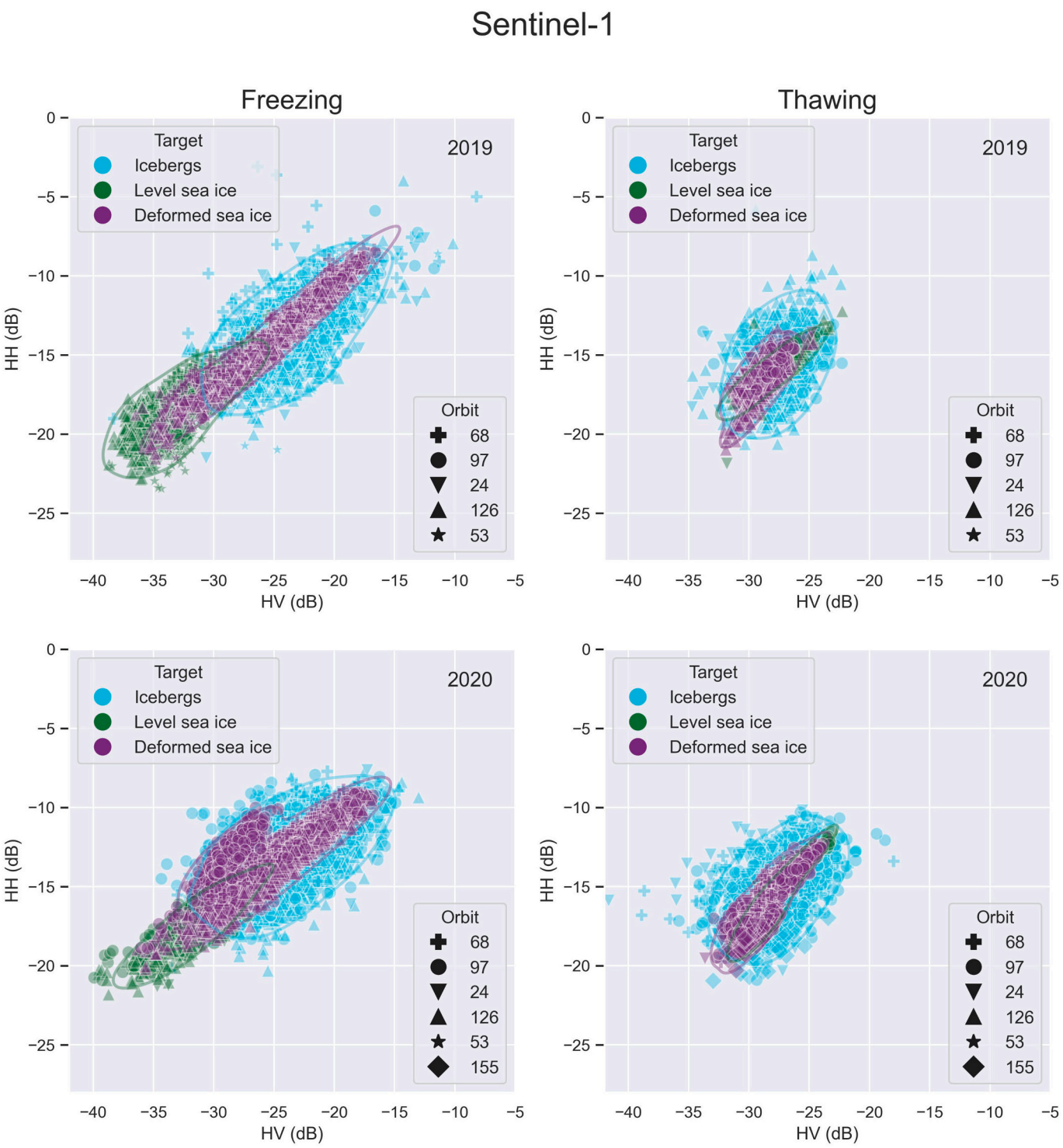

Fig. 7. Sentinel-1 backscattering intensities for all icebergs and their background of deformed or level ice for 2019 (top row), and 2020 (bottom row), and for both freezing (left) and thawing (right) conditions.

conditions, while the right column shows the data under thawing conditions. Fig. 8 is organized similarly for ALOS-2 (L-band).

It should be mentioned that since we merge data from different orbits without applying any form of incidence angle correction, we expect the scatter plots to exhibit a higher overall variance than if the data points were corrected to a common incidence angle. This is especially true for ALOS-2, which, as shown above, appears more sensitive to the incidence angle than C-band. To account for this, we have added orbit markers to the observations to make the interpretation easier.

In addition to the figures, we have also summarized the results for Sentinel-1 in Table 2 and for ALOS-2 in Table 3. Here, we show the slope (m) and Pearson correlation coefficient (ρ) of fitting a linear model to the data points, and additionally the mean (μ) and standard deviation (σ) are shown for HH and HV polarization respectively. The data have been separated into freezing and thawing seasons similarly to the figures and show the results for each of the three classes separately, i.e., icebergs (IB), level sea ice (LSI), and deformed sea ice (DSI).

Inspection of both the figures and the tables reveals that there is a

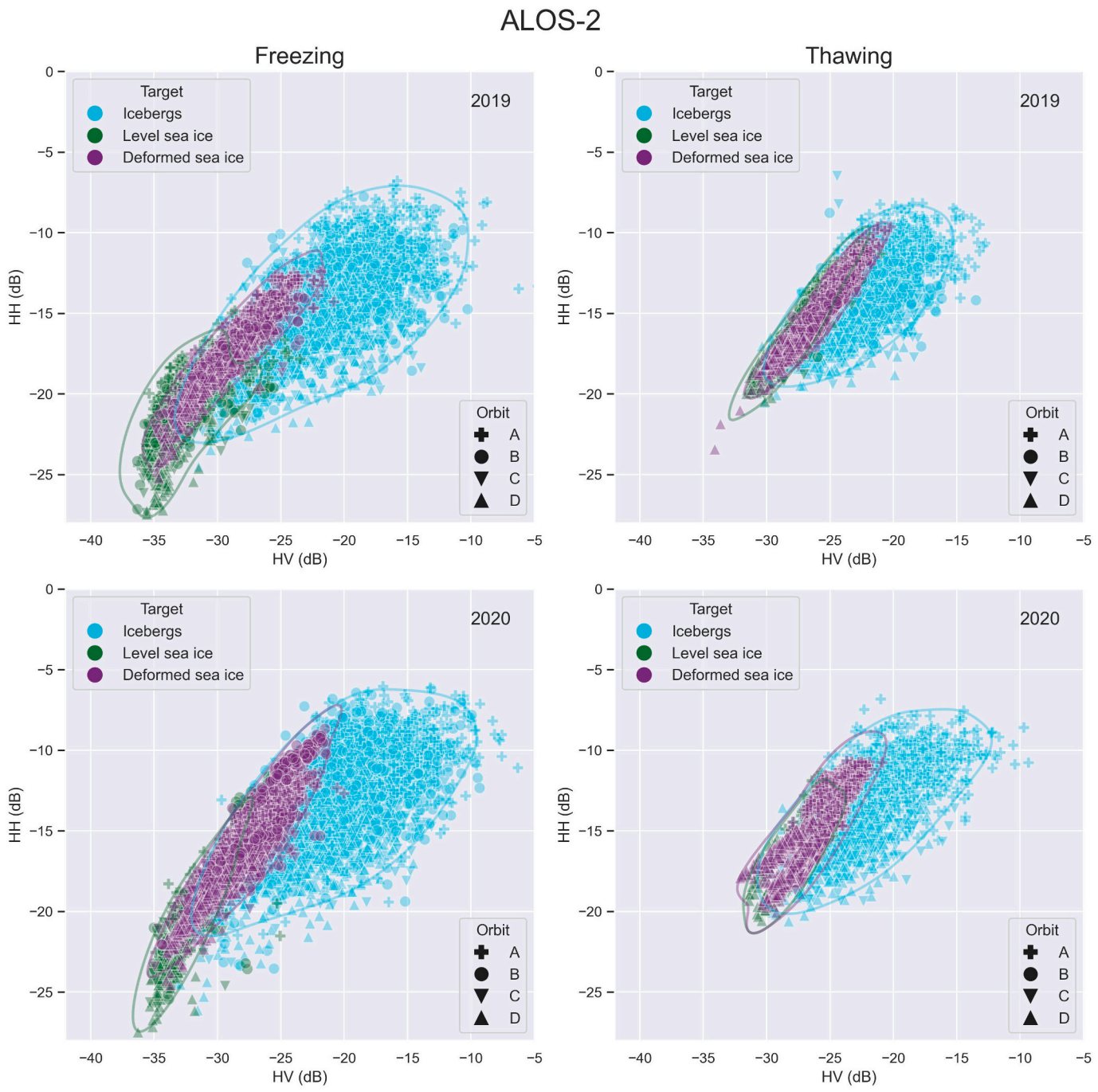

Fig. 8. ALOS-2 backscattering intensities for all icebergs and their background of deformed or level ice for 2019 (top row), and 2020 (bottom row), and for both freezing (left) and thawing (right) conditions.

high similarity between the data collected from 2019 and 2020. This is seen for both Sentinel-1 and ALOS-2, and for both freezing and thawing conditions. It is most evident for the mean backscatter (μ) and standard deviation (σ) in Tables 2 and 3. The mean backscatter typically varies around 1–2 dB for both C- and L-band, for both years, and seasons, and for all three classes. This is within a single standard deviation which is between 1 and 4 dB. These large similarities between the two years suggests that the results are of general validity in the AOI also for other years. However, inspection of the figures does reveal some minor inconsistencies. For Sentinel-1, we see a large subclass from orbit 97 in 2020 under freezing conditions, with lower HV and higher HH intensity than the average. Similarly, a subclass of higher HH scattering is seen for ALOS-2, freezing conditions for 2020, acquired from orbit B. These two cases are likely caused by precipitation, which is further detailed in Section 5.3 Other minor difference between the years can likely be attributed to the fact that the images used in the study cover slightly different periods, with different temporal gaps in the timeseries as seen in Figs. 5 and 6. In addition, it is expected that local ice conditions may vary slightly between the years, which could explain some of the differences between the years.

Both sea ice classes generally exhibit a strong correlation between HH and HV polarization. This is visible both in Figs. 7 and 8 and in Tables 2 and 3, with a correlation coefficient above 0.7 for both sea ice types and seasons for Sentinel-1, and above 0.6 for ALOS-2. The high correlation between HH and HV bands for level and deformed sea ice is consistent with results reported in the literature (Dierking, 2010;

Table 2
Main parameters characterizing the backscatter intensity for Sentinel-1. The slope (m), Pearson correlation coefficient (ρ), mean (μ) and standard deviation (σ) are calculated for each of the three classes icebergs (IB), level sea ice (LSI), and deformed sea ice (DSI), for 2019 and 2020. The results are separated according to freezing and thawing conditions.

Sentinel-1												
	2019						2020					
	Freezing			Thawing			Freezing			Thawing		
	IB	LSI	DSI	IB	LSI	DSI	IB	LSI	DSI	IB	LSI	DSI
m	0.46	0.49	0.65	0.38	0.58	0.68	0.36	0.52	0.47	0.36	0.89	0.84
ρ	0.66	0.73	0.97	0.38	0.89	0.70	0.58	0.88	0.85	0.46	0.92	0.86
μ_{hh}	−13.22	−18.65	−13.23	−15.57	−16.17	−16.79	−12.87	−17.70	−13.00	−15.06	−15.79	−16.52
μ_{hv}	−23.04	−33.25	−23.86	−27.49	−28.16	−29.21	−23.22	−32.01	−24.29	−27.46	−27.80	−29.06
σ_{hh}	1.99	1.59	2.49	1.81	1.06	1.18	1.83	1.85	1.84	1.77	2.00	1.54
σ_{hv}	2.85	2.37	3.72	1.82	1.64	1.21	2.98	3.10	3.34	2.27	2.07	1.58

Table 3
Main parameters characterizing the backscatter intensity for ALOS-2. The slope (m), Pearson correlation coefficient (ρ), mean (μ) and standard deviation (σ) are calculated for each of the three classes icebergs (IB), level sea ice (LSI), and deformed sea ice (DSI), for 2019 and 2020. The results are separated according to freezing and thawing conditions.

ALOS-2												
	2019						2020					
	Freezing			Thawing			Freezing			Thawing		
	IB	LSI	DSI	IB	LSI	DSI	IB	LSI	DSI	IB	LSI	DSI
m	0.45	0.63	0.81	0.53	1.05	0.94	0.46	1.23	1.02	0.51	0.94	0.95
ρ	0.65	0.63	0.92	0.68	0.94	0.95	0.65	0.86	0.93	0.70	0.79	0.84
μ_{hh}	−14.61	−21.58	−17.35	−14.16	−16.20	−15.10	−13.45	−20.43	−16.14	−13.81	−16.48	−15.16
μ_{hv}	−21.46	−33.29	−28.82	−22.82	−27.75	−25.97	−20.85	−32.01	−28.00	−22.40	−27.93	−26.52
σ_{hh}	2.99	1.97	2.11	2.24	2.26	1.90	3.02	3.37	2.74	2.50	2.30	2.26
σ_{hv}	4.38	1.97	2.42	2.91	2.03	1.93	4.25	2.36	2.50	3.47	1.94	2.00

Dierking and Wesche, 2014). The correlation for the iceberg class is much lower, with a correlation coefficient for Sentinel-1 between 0.58 and 0.66 for freezing conditions, and between 0.38 and 0.46 for thawing conditions. For ALOS-2, the correlation for the iceberg class is slightly higher, with values between 0.65 and 0.70 for both seasons. The lower correlation for icebergs may be explained by complex scattering mechanisms caused by the highly variable geometry at different spatial scales, which is typical for many icebergs. In our investigation, we did not separate icebergs according to their sizes and types (the latter cannot be characterized from satellite images). One has also to consider that the iceberg polygons obtained from Sentinel-2 images might not completely align with the positions of the SAR backscatter returns, causing additional variations in the results of the backscatter intensity. Another factor to consider is the varying window size used to estimate the average backscatter values. The iceberg backscatter is generally estimated in smaller windows than the sea ice backscatter as mentioned earlier, which will lead to a higher variance.

Under freezing conditions, we obtain a much higher correlation coefficient for deformed sea ice than for level sea ice. This is both evident in Figs. 7 and 8, and in Tables 2 and 3. For ALOS-2, the correlation coefficient is 0.63 for level sea ice and 0.92 for deformed sea ice for 2019, and 0.86 and 0.93 for 2020, while for Sentinel-1 the correlation coefficient is 0.73 for level sea ice and 0.97 for deformed sea ice for 2019. For 2020, the trend of higher correlation for deformed sea ice is not equally visible for Sentinel-1, with correlation coefficients of 0.88 and 0.85 for level and deformed sea ice respectively. This lower correlation for deformed sea ice in 2020 might be due to the influence of precipitation during acquisitions on orbit 97 mentioned earlier. In general, the lower correlation coefficient for level sea ice during freezing conditions might be caused by the overall lower backscatter intensity of this ice type, which is around -33 dB for both ALOS-2 and Sentinel-1 in the HV band. These low backscatter intensities are at the noise level (and below the nominal average NESZ for ALOS-2 as seen in Table 1), which decreases the linear correlation coefficient. For ALOS-2, the measurements also appear to show a cut-off of HV values around -35 dB as seen in the left row of Fig. 8 We do not know the exact reason, but the most presumable cause is that it is related to the noise level.

Regarding the influence of melt onset on the backscatter of the sea ice classes, the greatest impact for Sentinel-1 appears to be the increase in backscatter for level sea ice, with an increase of around 2 dB for the HH band and 5 dB for the HV band, and the decrease of backscatter from deformed sea ice, of around 3 dB for HH and 5 dB for HV. This means that the two sea ice classes converge towards the same average backscatter under thawing conditions, at around -16 dB for the HH band and -28 dB for the HV band, and with similar slopes and correlation coefficient as well. For Sentinel-1, the melt onset also gives rise to a lower variance of the sea ice classes. This can be attributed to an increase of scattering from larger brine-wetted snow grains on level ice and a slight decrease in backscatter from deformed (older) ice because of reduced penetration into the ice volume, all in all leading to similar backscatter from both level and deformed sea ice (Casey et al., 2016). As the stage of the melt advances later in the season, we expect that the wet ice surface gives rise to a dominance of surface scattering. The similarity of backscattering between the sea ice classes can also be seen in Fig. 2, where the two sea ice classes become indistinguishable in the two images acquired later in the season compared to the image acquired early in the season. A similar observation was reported by Yackel et al. (2007), where for melt onset, the backscatter for first-year ice (FYI) was reported as being higher than for multi-year ice (MYI) for C-band SAR. For ALOS-2, the level sea ice class shows an increase in backscatter after melt onset of around 5 dB for both HH and HV. The corresponding numbers for deformed sea ice are 1-2 dB for HH and 2-3 dB for HV. Hence the two sea ice classes become less separable also at L-band after melt onset, with similar mean backscatter, variance, and slope under melting conditions for the two sea ice types.

Looking at the iceberg class, there appears to be a smaller influence of thawing conditions on ALOS-2 imagery compared to Sentinel-1. For Sentinel-1, the mean backscatter for icebergs decreases by around 2 dB

for the HH band and 4 dB for the HV band at the onset of melting conditions, while for ALOS-2 the HH band is unaltered by the melt onset while the HV band shows a decrease around 1 dB after melt onset. The slope and correlation coefficient for ALOS-2 is also more stable for the iceberg class after the melt onset compared to Sentinel-1. This could be caused by the higher penetration depth of L-band, making ALOS-2 less influenced by wet snow or water on the iceberg's surfaces compared to C-band. For both Sentinel-1 and ALOS-2, there is a slight decrease in standard deviation after the onset of melt, which is most significant for ALOS-2.

Sentinel-1 shows a consistent large overlap between the iceberg and sea ice backscattered intensities (Fig. 7). For freezing conditions, the overlap is especially large between the iceberg and deformed sea ice class, while there is still good separation between the iceberg and level sea ice class. For thawing conditions, there is a large overlap between the iceberg class and both sea ice classes. These observations compare well with the observations from Section 4.1 and demonstrates that it is very difficult to determine intensity thresholds for separating sea ice and iceberg radar responses using C-band SAR. For ALOS-2, the intensities of the iceberg class are consistently shifted towards higher HV backscatter compared to both sea ice classes for both freezing and thawing conditions. This can also be seen in Fig. 2, where the iceberg in the subset is consistently visible as red (HV) blobs.

This enables us to separate icebergs and sea ice more easily using L-band than at C-band, suggesting that L-band is better suited for detecting icebergs in sea ice. Preferably the separation should be done using a combination of HH- and HV-polarizations. And separation is easier under freezing conditions.

4.3. CFAR results

The results of the CFAR detector outlined in Section 3.5 is shown in Tables 4 and 5 for Sentinel-1 and ALOS-2 respectively. In addition, a small subset of the results is shown in Fig. 9, giving an impression of the quality of automatic iceberg detection by separating the true positives (green), false detections (red), and missed detections (yellow).

We found that for 2019, Sentinel-1 has a decent precision (0.67) and recall (0.57) for icebergs in level sea ice, and a poor precision (0.21) and recall (0.07) for icebergs in deformed sea ice (Table 4). For 2020, the results are even worse with a precision and recall for level sea ice at 0.23 and 0.42 respectively, and 0.06 and 0.06 respectively for deformed sea ice. This is also reflected in the number of false positives and false negatives, with a very high number of false negatives in deformed sea ice for 2019, and a high number of both false positives and negatives for deformed sea ice in 2020. The results show that Sentinel-1 under some conditions performs well in detecting icebergs in level sea ice, although with a high number of false negatives in 2019 and a high number of false positives in 2020. For deformed sea ice, Sentinel-1 generally performs very poor, with a very low number of true positives compared to the number of false positives and negatives. This is also obvious from Fig. 9, where Sentinel-1 has not been able to detect any of the icebergs in deformed sea ice.

The results for ALOS-2 in Table 5 shows better results across all scores, with a precision above 0.9 for both sea ice types in 2019, and a decent recall as well. For 2020, the results are slightly worse, but still better than for Sentinel-1, with a precision above 0.75 and recall at 0.65 and 0.49 for level and deformed sea ice respectively. ALOS-2 thus shows much better performance for detecting icebergs in both level and deformed sea ice, with a much higher number of true positives, and lower number of false positives and negatives.

Table 4
Results of applying the CFAR algorithm to two Sentinel-1 (C-band) images from the spring of 2019 and 2020 respectively.

	Sentinel-1					
	2019-04-27			2020-04-27		
	Level SI	Deformed SI	Total	Level SI	Deformed SI	Total
FP	82	162	244	198	670	868
FN	126	543	669	83	721	804
TP	166	44	210	59	46	105
Precision	0.67	0.21	0.46	0.23	0.06	0.11
recall	0.57	0.07	0.24	0.42	0.06	0.12

Table 5
Results of applying the CFAR algorithm to two ALOS-2 (L-band) images from the spring of 2019 and 2020 respectively.

	ALOS-2					
	2019-04-27			2020-04-27		
	Level SI	Deformed SI	Total	Level SI	Deformed SI	Total
FP	13	26	39	20	127	147
FN	95	347	442	50	394	444
TP	196	241	437	92	373	465
Precision	0.94	0.90	0.92	0.82	0.75	0.76
recall	0.67	0.41	0.50	0.65	0.49	0.51

Although ALOS-2 shows significantly better results than Sentinel-1, a considerable number of icebergs were not detected, with the total number of false negatives being comparable with the number of true positives. Further investigation revealed that the detection accuracy increased with increasing iceberg size, and visual inspection of the results revealed that many of the missed detections were found in places where icebergs were located in clusters, as e.g., seen in the top right and right side of Fig. 9. This suggests that some of the false negatives could be due to the CFAR detector falsely interpreting spots of high areal iceberg densities as background clutter, thus lowering the probability of detection in these areas. These types of errors could be avoided in the future by truncating high intensity pixels (Tao et al., 2016). The clusters of icebergs often originate from a break-up of a single larger iceberg, where the broken pieces remain closely together because of the surrounding fast ice or because they are grounded. This will less likely occur for icebergs moving in drifting sea ice. Inspection of Fig. 9 also reveals that many of the missed detections are icebergs of medium size which means that perhaps the performance could be further increased by tuning the probability of false alarm rate or the window size of the CFAR detector. We expect that better performance can be achieved by applying the detector to the data in the original pixel spacing (25 m), instead of the down-sampled data (40 m), which we use here to match the Sentinel-1 resolution. Seen from the perspective of operational iceberg monitoring, the large number of missed detections gives cause for concern and needs to be investigated in more detail. This, however, was beyond the scope of this study.

5. Summary

Comparison of both the timeseries contrast plots (Figs. 5 and 6), and the scatterplots (Figs. 7 and 8), shows a large similarity between the data gathered from 2019 and 2020. This suggests that the results are of general validity for the investigated area, with some small inconsistencies which we attribute to the different meteorological conditions and temporal gaps in our timeseries.

Figures 5 to 8 and Tables 2 and 3 all suggest that Sentinel-1 (C-band) only offers a satisfactory separability between level sea ice and icebergs under freezing conditions and not under thawing conditions. Additionally, Sentinel-1 is not able to distinguish between icebergs and deformed sea ice at all, which also suggests that small floes of deformed sea ice embedded in level sea ice could be misinterpreted as icebergs when using C-band for iceberg detection.

ALOS-2 on the other hand, can distinguish between icebergs in both level and deformed sea ice, and although the performance is much higher under freezing conditions, the classes can still be separated under thawing conditions as well.

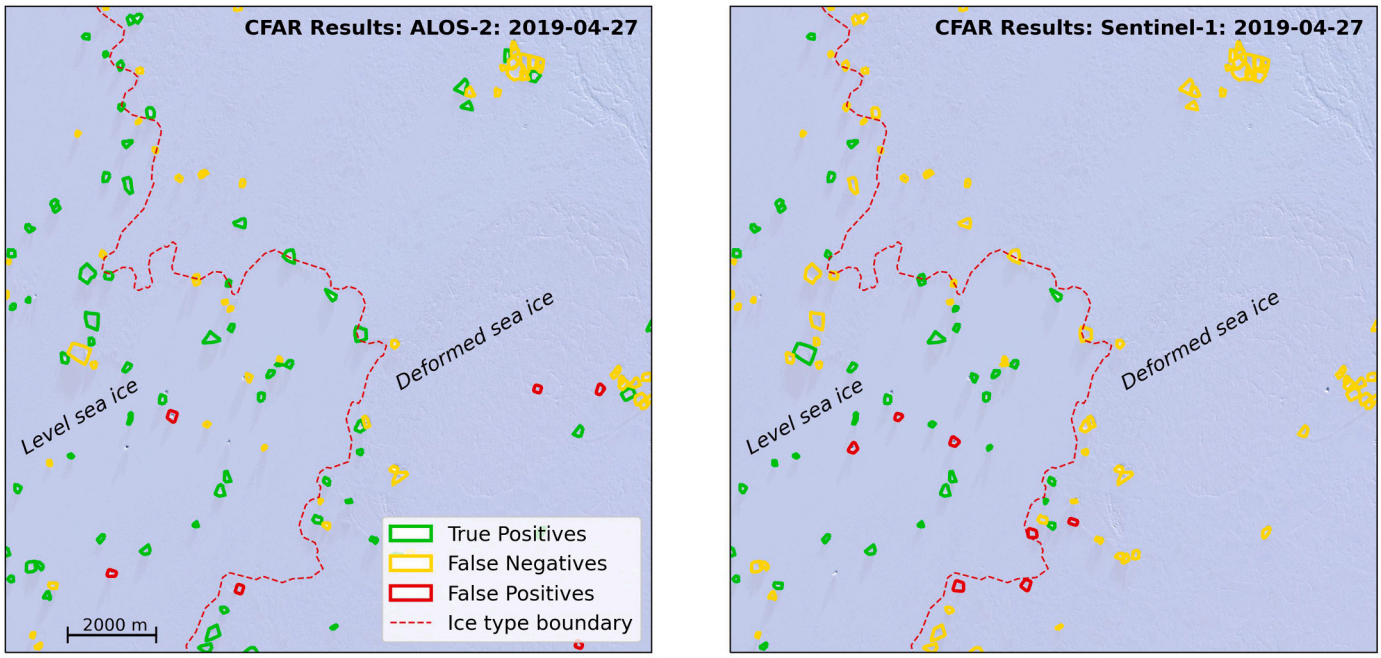

Fig. 9. Results of running the iceberg detection algorithms on the ALOS-2 L-band images (left), and the Sentinel-1C-band image (right) overlaid on a Sentinel-2 image. Detected icebergs are marked with green, false detections with red, and missed detections with yellow. (For interpretation of the references to colour in this figure legend, the reader is referred to the web version of this article.)

The results are further supported by comparing the performance of a CFAR detection algorithm run on two C-band and two L-band images all acquired during the spring. Here, we also saw that L-band offered a much better performance than C-band for detecting icebergs in sea ice. All in all, the results suggest that L-band SAR is superior for detecting icebergs in areas with sea ice if compared to C-band. Furthermore, to minimize misclassifications, a detector designed for finding icebergs in L-band SAR images should be based on a combination of HH- and HV-polarization rather than applying separate thresholds to the two polarizations.

6. Discussion

6.1. Automatic matching of the L-band time delay

Validating backscatter values from icebergs at L-band was only possible by considering time-delayed reflections. As noted in Section 3.3, the time delay depends on, e.g., geometry, dielectric properties, and internal structure of an iceberg, and the presence of water or wet snow on the surface. To account for the time delay when collecting validation data, we opted for a pragmatic approach by shifting the iceberg polygon down-range to a location that maximizes the HV backscatter return. An issue with this approach is that if iceberg radar returns are too weak to be distinguishable from the surrounding sea ice, we risk finding and including local maxima caused by sea ice scattering, and thus artificially increasing the average contrast, especially during the thawing season, when the sea ice backscatter for level sea ice is increased. This will give rise to a bias of the HV backscatter for icebergs – moving some of the ALOS-2 iceberg samples towards the right in Fig. 8, which will influence the overall contrast. To account for this, we performed a visual inspection of the SAR images with the focus on the time-delayed polygons of icebergs that were determined from the Sentinel-2 image. This inspection revealed that a majority of the corrected polygons overlapped with distinct backscatter maxima that could be distinguished from the surrounding sea ice backscatter, and therefore was interpreted as coming from the icebergs. Based on the visual inspection, we have confidence that this bias does not change the overall conclusion of the results; namely that L-band is preferable to C-band.

6.2. Variation of contrast as a function of incidence angle for L-band

From Fig. 6 it is evident that the backscatter contrast and the orbit of ALOS-2 are related, since orbits A and B exhibit a generally higher contrast than orbits C and D. This is most likely caused by the differences in incidence angles covering the AOI between the orbits (see Fig. 1) and different sensitivities (slopes) of the sea ice and the iceberg backscatter to changes in incidence angle. The fact that we do not see a similar response at C-band may indicate that the sensitivities of the backscattered intensities from sea ice and icebergs are similar, causing less variation in the contrast for varying incidence angles. As mentioned in Section 2.2, the ALOS-2 data were delivered without incidence angle information. Therefore, a thorough investigation of the influence of incidence angle on the contrast at L-band cannot be performed at this stage.

6.3. Influence of precipitation

In Fig. 7, for Sentinel-1 during freezing conditions in 2020, a cluster of deformed sea ice data from orbit 97 is recognized that reveals an increase in HH and a decrease in HV compared to the other observations. A detailed investigation showed that these outliers come from an image that was acquired on May 25th, 2020, which coincides with a precipitation event observed at the Danmarkshavn weather station (Fig. 1) on May 24th, when 24 mm of precipitation was recorded. This appears to have influenced the ALOS-2 observations as well, with an increase in both HH and HV. This can be recognized in Fig. 8 for orbit B. The corresponding image was acquired on May 25th. Based on the temperature on May 24th, 2020, the precipitation was likely in the form of rain or possibly wet snow.

The rest of the period (April–July) for both 2019 and 2020 saw very little precipitation. The monthly average for April–July 2019 was below 10 mm, and for 2020 both April and June were below 10 mm, whereas in May and July the monthly precipitation was 32 and 21 mm, respectively.

6.4. Influence of acquisition times

The Sentinel-1 overpasses covering our AOI took place in the morning (08:00–08:30 UTC) and the ALOS-2 overpasses in the early afternoon (13:45–14:30 UTC), i.e., with a 6-h time difference. The temperature variation in the area (shown as the shaded red area in Figs. 5 and 6) is at around 6oC for a 24-h period. With this relatively large temperature difference, Sentinel-1 images were most probably acquired under conditions where it is several degrees colder than during ALOS-2 data takes. In the transition period between freezing and thawing conditions, C-band images may have been acquired during freezing, and L-band during thawing conditions. However, since quick temperature changes will mainly influence the surface layer of the snow, and since L-band is less sensitive to the surface layer, we expect that this temperature difference will not significantly affect our results.

6.5. Advanced melt

There are some minor indications that the contrast for C-band increases during advanced stages of melt. This can be observed in Fig. 5, where the contrast towards the end of the time series is around 2 dB for both polarizations and for both level and deformed ice. This can also be observed in Fig. 2 (for the 2019-07-08 acquisition), where the icebergs at C-band appear to have a slightly higher backscatter level than the sea ice, although still exhibiting a lower contrast than at L-band. However, due to the break-up of the fast ice at the end of July for both 2019 and 2020, we could not investigate the development of contrast further into the more advanced stages of the melt.

6.6. Operational iceberg detection

As we saw in Section 4.1, some orbits appeared to give a higher contrast between the icebergs and sea ice classes compared to other orbits, especially for ALOS-2 (L-band). Therefore, we expect that the orbit selection influences the performance of the CFAR detector. Due to the lack of incidence angle data for the ALOS-2 images we could not investigate this effect in depth. For our CFAR detection results, the first ALOS-2 image was acquired from orbit D, and the second from orbit B. Here, orbit D results in a relatively low contrast between icebergs and sea ice, while B gives a high contrast. For comparison, both Sentinel-1 images were acquired from orbit 126, which were shown to give a relatively high contrast, although the influence of the acquisition orbit is not so pronounced at C-band compared to L-band. Since the performance of L-band was much higher than C-band for both orbits, we do not expect that the conclusions change significant for acquisitions from different orbits.

It should, however, be mentioned that the equivalent number of looks (ENL) is different for the two sensors, which might affect the results. The ENL of Sentinel-1 in EW mode is around 10.7 (Bourbigot et al., 2016), whereas the ENL for ALOS-2 is not provided but probably smaller than the multi-look value of 6 (Table 1). This will likely affect the results as the ALOS-2 images are expected to have a slightly higher level of speckle noise. Nevertheless, the L-band image is proving to be clearly superior to C-band, so we do not expect that an ENL similar for both sensors change the results significantly.

6.7. Extending the results for detecting icebergs in drift ice

To accurately validate our results and consider temporal variations of radar backscattering, we were restricted to using a dataset consisting of stationary icebergs in land-fast sea ice because optical and radar images over a given area were only available with considerable time gaps. Nevertheless, we expect that our conclusions are also valid for detecting icebergs in drifting sea ice – at least for the sea ice types that we have focused on in this study. However, special cases may require additional analyses, such as icebergs embedded in brash ice, pancake ice, or in ice covered with frost flowers.

7. Conclusion

In this study, we have compared a time series of dual-pol L- and C-band SAR images acquired over the fast-ice at Belgica Bank, North-Eastern Greenland, during 2019 and 2020 with the objective to assess the detectability of medium and large icebergs under different seasonal conditions. Using Sentinel-2 as an independent reference, backscattering intensities from several hundred stationary icebergs, as well as from the sea ice surrounding them, were extracted, and the intensity contrast between level and deformed sea ice, on one hand, and icebergs, on the other hand, was calculated for the freezing and thawing seasons.

The results showed that at both freezing and thawing conditions, C-band cannot differentiate between deformed sea ice and icebergs. Icebergs in level ice can mostly be detected in C-band images acquired under freezing conditions; however, small, deformed floes in level sea ice might be misinterpreted as icebergs. The usefulness of Sentinel-1 for mapping icebergs in icy waters is therefore limited, and we expect similar results for other C-band satellites such as RADARSAT.

L-band, on the other hand, reveals a considerable better separation of icebergs in both deformed and level sea ice under freezing conditions. Under thawing conditions, the L-band contrast generally decreases, but a high number of icebergs still exhibit a sufficiently high contrast for a successful detection. Furthermore, we observed a significant incidence angle dependency of the iceberg and sea ice contrast at L-band which suggests that icebergs should be mapped at low incidence angles. Overall, L-band SAR offers a large advantage over C-band for mapping medium and large icebergs in sea ice.

Our findings were verified by applying a simple CFAR detection algorithm to two pairs of C- and L-band images for which 879 and 909 icebergs for the first and second pair, respectively, were identified in a corresponding Sentinel-2 image for validation. Using C-band, we found that around 24% of the icebergs were accurately detected, against 50% detected icebergs using L-band for the first image pair, while the second image pair showed only 11% detected icebergs for C-band and 51% for L-band. Additionally, C-band showed around six times as many false detections compared to L-band. However, we also noted a large number of missed icebergs at both frequencies, especially at locations of iceberg clusters This, however, may be largely attributed to the simplicity of the test, with a fixed clutter geometry. We expect that more advanced methods may solve this problem.

By using a large number of icebergs as validation data, and a time series of images covering the freezing/thawing seasons for two separate years, we expect that the results can be generalized for most Arctic conditions. The results shown here demonstrate that icebergs in regions with sea ice should be preferably detected using L-band SAR at low incidence angles. Further, an iceberg detector should be designed to use both HH and HV polarization for achieving best results. Our findings will help advancing the monitoring of icebergs in sea ice using SAR, which is beneficial to both maritime safety and for evaluating the impact of ice discharge on the oceans.

Funding

This research was funded by CIRFA partners and the Research Council of Norway (grant number 237906).

CRediT authorship contribution statement

Laust Færch: Writing – original draft, Visualization, Software, Methodology, Formal analysis. **Wolfgang Dierking:** Writing – review & editing, Supervision, Methodology, Conceptualization. **Nick Hughes:** Writing – review & editing, Supervision, Resources. **Anthony P. Doulgeris:** Writing – review & editing, Supervision, Methodology.

Declaration of competing interest

The authors declare that they have no known competing financial interests or personal relationships that could have appeared to influence the work reported in this paper.

Data availability

Data will be made available on request.

Acknowledgement

ALOS-2/PALSAR-2 data are provided by JAXA through the 2019 to 2022 mutual cooperation project between ESA and JAXA on Using Synthetic Aperture Radar Satellites in Earth Science and Applications. We are also thankful for the support received by the ESA and the Ministry of Science and Technology (MOST) of the P.R. China through the Dragon-5 cooperation. And we are also thankful for the discussions with our Chinese partners.

References

Achanta, R., Shaji, A., Smith, K., Lucchi, A., Fua, P., Süsstrunk, S., 2012. SLIC Superpixels compared to state-of-the-art Superpixel methods. IEEE Trans. Pattern Anal. Mach. Intell. 34 (11), 2274–2282. https://doi.org/10.1109/TPAMI.2012.120.

Amdal, F., Hughes, N., 2022. Multi-Sensor Ice Analysis Data: Analysis for Belgica Bank, North East Greenland 2019-20 (1.0.0) [Data set]. Zenodo. https://doi.org/10.5281/zenodo.7053975.

Arndt, E.J., Jokat, W., Dorschel, B., Myklebust, R., Dowdeswell, J.A., Evans, J., 2015. A new bathymetry of the Northeast Greenland continental shelf: constraints on glacial and other processes. Geochem. Geophys. Geosyst. 18, 1541–1576. https://doi.org/10.1002/2015GC005931.Received.

Bailey, J., Marino, A., 2020. Quad-polarimetric multi-scale analysis of icebergs in ALOS-2 SAR data: a comparison between icebergs in west and East Greenland. Remote Sens. 12 https://doi.org/10.3390/rs12111864.

Bailey, J., Marino, A., Akbari, V., 2021. Comparison of target detectors to identify icebergs in quad-Polarimetric L-band synthetic aperture radar data. Remote Sens. 13.

Barbat, M.M., Rackow, T., Hellmer, H.H., Wesche, C., Mata, M.M., 2019. Three years of near-coastal Antarctic iceberg distribution from a machine learning approach applied to SAR imagery. J. Geophys. Res. Ocean. 124, 6658–6672. https://doi.org/10.1029/2019JC015205.

Bigg, G., 2015. Icebergs: Their Science and Links to Global Change. Cambridge University Press, Cambridge. https://doi.org/10.1017/CBO9781107589278.

Bourbigot, M., Johnson, H., Piantanda, R., 2016. Sentinel-1 Product Definition. ESA. https://sentinels.copernicus.eu/web/sentinel/user-guides/sentinel-1-sar/document-library/-/asset_publisher/1dO7RF5fJMbd/content/sentinel-1-product-definition (last access: 6 December 2023).

Braakmann-Folgmann, A., Shepherd, A., Hogg, D., Redmond, E., 2023. Mapping the extent of giant Antarctic icebergs with deep learning. Cryosph. 17, 4675–4690. https://doi.org/10.5194/tc-17-4675-2023.

Bügelmayer, M., Roche, D.M., Renssen, H., 2015. How do icebergs affect the Greenland ice sheet under pre-industrial conditions? - a model study with a fully coupled ice-sheet-climate model. Cryosphere 9, 821–835. https://doi.org/10.5194/tc-9-821-2015.

Buus-Hinkler, J., Qvistgaard, K., Krane, K.A.H., 2014. Iceberg number density - reaching a full picture of the Greenland waters. Int. Geosci. Remote Sens. Symp. 270–273. https://doi.org/10.1109/IGARSS.2014.6946409.

Casey, J.A., Howell, S.E.L., Tivy, A., Haas, C., 2016. Separability of sea ice types from wide swath C- and L-band synthetic aperture radar imagery acquired during the melt season. Remote Sens. Environ. 174, 314–328. https://doi.org/10.1016/j.rse.2015.12.021.

Copernicus Marine Service, 2023. SAR Sea Ice Berg Concentration and Individual Icebergs Observed with Sentinel-1. 10.48670/moi-00129.

Danish Meteorological Institute, 2023. Vejrarkiv. https://www.dmi.dk/vejrarkiv/ (Accessed 2023-08-10).

Das, A., Kumar, R., Rosen, P., 2021. Nisar mission overview and updates on ISRO science plan. In: 2021 IEEE India Geosci. Remote Sens. Symp. InGARSS 2021 - Proc, pp. 269–272. https://doi.org/10.1109/InGARSS51564.2021.9791979.

Davidson, M., Gebert, N., Giulicchi, L., 2021. ROSE-L – the L-band SAR mission for copernicus. In: Proc. Eur. Conf. Synth. Aperture Radar, EUSAR 2021-March, pp. 236–237.

Dierking, W., 2010. Mapping of different sea ice regimes using images from sentinel-1 and ALOS synthetic aperture radar. IEEE Trans. Geosci. Remote Sens. 48, 1045–1058. https://doi.org/10.1109/TGRS.2009.2031806.

Dierking, W., 2020. In: Di Martino, G., Iodice, A. (Eds.), Sea Ice And Icebergs. Maritime Surveillance with Synthetic Aperture Radar. Institution of Engineering and Technology, p. 346. ISBN 9781785616013. https://doi.org/10.1049/SBRA521E.

Dierking, W., Davidson, M., 2020. Enhanced Sea ICE monitoring at L- and C-bands using Rose-L and Sentinel-1. Int. Geosci. Remote Sens. Symp. 4059–4060 https://doi.org/10.1109/IGARSS39084.2020.9323886.

Dierking, W., Wesche, C., 2014. C-band radar polarimetry - useful for detection of icebergs in sea ice? IEEE Trans. Geosci. Remote Sens. 52, 25–37. https://doi.org/10.1109/TGRS.2012.2234756.

Evans, B., Faul, A., Fleming, A., Vaughan, D.G., Hosking, J.S., 2023. Unsupervised machine learning detection of iceberg populations within sea ice from dual-polarisation SAR imagery. Remote Sens. Environ. 297, 113780 https://doi.org/10.1016/j.rse.2023.113780.

Færch, L., Dierking, W., Hughes, N., Doulgeris, A.P., 2023. A comparison of CFAR object detection algorithms for iceberg identification in L-and C-band SAR imagery of the Labrador Sea. Cryosph. 17, 5335–5355.

Ferdous, M.S., McGuire, P., Power, D., Johnson, T., Collins, M.J., 2018. A comparison of numerically modelled iceberg backscatter signatures with Sentinel-1 C-band synthetic aperture radar acquisitions. Can. J. Remote. Sens. 44, 232–242. https://doi.org/10.1080/07038992.2018.1495554.

Ferdous, M.S., Himi, U.H., McGuire, P., Power, D., Johnson, T., Collins, M.J., 2019. C-band simulations of melting icebergs using GRECOSAR and an em model: varying wind conditions at lower beam mode. IEEE J. Sel. Top. Appl. Earth Obs. Remote Sens. 12, 5134–5146. https://doi.org/10.1109/JSTARS.2019.2954847.

Gill, R.S., 2001. Operational detection of sea ice edges and icebergs using SAR. Can. J. Remote. Sens. 27, 411–432. https://doi.org/10.1080/07038992.2001.10854884.

Gillies, S., et al., 2013. Rasterio: geospatial raster I/O for Python programmers. URL. https://github.com/rasterio/rasterio. Giraldez, 2004.

Giraldez, Alberto E., 2004. SAOCOM-1 Argentina L-band SAR mission overview. ESA Special Publication 565, 27.

Gray, A.L., Arsenault, L.D., 1991. Time-delayed reflections in L-band synthetic aperture radar imagery of icebergs. IEEE Trans. Geosci. Remote Sens. 29, 284–291. https://doi.org/10.1109/36.73670.

Guo, W., Itkin, P., Lohse, J., Johansson, M., Doulgeris, A.P., 2022. Cross-platform classification of level and deformed sea ice considering per-class incident angle dependency of backscatter intensity. Cryosphere 16, 237–257. https://doi.org/10.5194/tc-16-237-2022.

Haas, C., 2001. The seasonal cycle of ERS scatterometer signatures over perennial Antartic Sea ice and associated surface ice properties and processes. Ann. Glaciol. 33, 69–73. https://doi.org/10.3189/172756401781818301.

Harris, C.R., Millman, K.J., van der Walt, S.J., Gommers, R., Virtanen, P., Cournapeau, D., Wieser, E., Taylor, J., Berg, S., Smith, N.J., Kern, R., Picus, M., Hoyer, S., van Kerkwijk, M.H., Brett, M., Haldane, A., del Río, J.F., Wiebe, M., Peterson, P., Gérard-Marchant, P., Sheppard, K., Reddy, T., Weckesser, W., Abbasi, H., Gohlke, C., Oliphant, T.E., 2020. Array programming with NumPy. Nature 585, 357–362. https://doi.org/10.1038/s41586-020-2649-2.

Hughes, N.E., Wilkinson, J.P., Wadhams, P., 2011. Multi-satellite sensor analysis of fast-ice development in the Norske Øer ice barrier, Northeast Greenland. Ann. Glaciol. 52, 151–160. https://doi.org/10.3189/172756411795931633.

International Ice charting Working Group, 2019. Task Team 8: Mariner Training Requirement. Technical Report. https://nsidc.org/sites/nsidc.org/files/files/noaa/iicwg/2019/IICWG_Mariner_Survey_Intermediate_Report.pdf (Accessed 2023-08-10).

Jakobsson, M., Mayer, L.A., Bringensparr, C., et al., 2020. The international bathymetric chart of the Arctic Ocean version 4.0. Sci Data 7, 176. https://doi.org/10.1038/s41597-020-0520-9.

JAXA, 2012. ALOS-2/PALSAR-2 Level 1.1/1.5/2.1/3.1 CEOS SAR Product Format Description. Technical Report. https://www.eorc.jaxa.jp/ALOS-2/en/doc/fdata/PALSAR-2_xx_Format_CEOS_E_r.pdf (Accessed 2023-08-10).

Jordahl, K., 2014. GeoPandas: Python Tools for Geographic Data. URL. https://github.com/geopandas/geopandas.

Kankaku, Y., Suzuki, S., Osawa, Y., 2013. ALOS-2 mission and development status. Int. Geosci. Remote Sens. Symp. 2396–2399 https://doi.org/10.1109/IGARSS.2013.6723302.

Kim, J., Kim, D., Kim, S., 2011. Iceberg Detection using full-polarimetric RADARSAT-2 SAR Data in West Antarctica Jin-Woo, 2011. In: 3rd International Asia-Pacific Conference on Synthetic Aperture Radar (APSAR). IEEE, pp. 236–239.

Koo, Y., Xie, H., Mahmoud, H., Iqrah, J.M., Ackley, S.F., 2023. Automated detection and tracking of medium-large icebergs from Sentinel-1 imagery using Google Earth Engine. Remote Sens. Environ. 296, 113731 https://doi.org/10.1016/j.rse.2023.113731.

Liu, C., 2015. A Dual-Polarization Ship Detection Algorithm. Defence Research and Development Canada. Ottawa, ON, Canada, Ottawa Research Centre.

Mahoney, A.R., 2018. Landfast Sea Ice in a Changing Arctic. Arctic report card, 99. https://arctic.noaa.gov/report-card/report-card-2018/landfast-sea-ice-in-a-changing-arctic/ (Accessed 2023-08-10).

Mankoff, K.D., Solgaard, A., Colgan, W., Ahlstrøm, A.P., Abbas Khan, S., Fausto, R.S., 2020. Greenland ice sheet solid ice discharge from 1986 through March 2020. Earth Syst. Sci. Data 12, 1367–1383. https://doi.org/10.5194/essd-12-1367-2020.

Marino, A., 2018. Iceberg detection with L-band ALOS-2 data using the Dual-Pol Ratio Anomaly Detector. In: Int. Geosci. Remote Sens. Symp. 2018-July, pp. 6067–6070. https://doi.org/10.1109/IGARSS.2018.8519206.

Marino, A., Dierking, W., Wesche, C., 2016. A depolarization ratio anomaly detector to identify icebergs in sea ice using dual-polarization SAR images. IEEE Trans. Geosci. Remote Sens. 54, 5602–5615. https://doi.org/10.1109/TGRS.2016.2569450.

Marson, J.M., Gillard, L.C., Myers, P.G., 2021. Distinct Ocean responses to Greenland's liquid runoff and iceberg melt. J. Geophys. Res. Ocean. 126, 1–18. https://doi.org/10.1029/2021JC017542.

Mazur, A.K., Wåhlin, A.K., Krężel, A., 2017. An object-based SAR image iceberg detection algorithm applied to the Amundsen Sea. Remote Sens. Environ. 189, 67–83. https://doi.org/10.1016/j.rse.2016.11.013.

Oliver, C., Quegan, S., 2004. Understanding Synthetic Aperture Radar Images. SciTech Publishing Inc., Raleigh, NC 27613 (ISBN 1-891121-31-6.).

Power, D., Youden, J., Lane, K., Randell, C., Flett, C.R.D., 2001. Iceberg detection capabilities of radarsat synthetic aperture radar. Can. J. Remote. Sens. 27, 476–486. https://doi.org/10.1080/07038992.2001.10854888.

Rignot, E., Echelmeyer, K., Krabill, W., 2014. Penetration Depth of Interferometric Synthetic-aperture Radar Signal in Snow and Ice Penetration Depth of Interferometric Synthetic-aperture Radar signals in SNOW and Ice. https://doi.org/10.1029/2000GL012484.

Sandven, S., Babiker, M., Kloster, K., 2007, April. Iceberg observations in the Barents Sea by radar and optical satellite images. In: Proceedings of the ENVISAT Symposium, Montreux, Switzerland (pp. 23-27).

Soldal, I.H., Dierking, W., Korosov, A.A., Marino, A., 2019. Automatic detection of small icebergs in fast ice using satellite wide-swath SAR images. Remote Sens. 11, 1–24. https://doi.org/10.3390/rs11070806.

Tao, D., Doulgeris, A.P., Brekke, C., 2016. A segmentation-based CFAR detection algorithm using truncated statistics. IEEE Trans. Geosci. Remote Sens. 54, 2887–2898. https://doi.org/10.1109/TGRS.2015.2506822.

van der Walt, Stéfan, Schönberger, Johannes L., Nunez-Iglesias, Juan, Boulogne, François, Warner, Joshua D., Yager, Neil, Gouillart, Emmanuelle, Yu, Tony, the scikit-image contributors, 2014. scikit-image: Image processing in Python. https://doi.org/10.7717/peerj.453.

Wesche, C., Dierking, W., 2012. Iceberg signatures and detection in SAR images in two test regions of the Weddell Sea, Antarctica. J. Glaciol. 58, 325–339. https://doi.org/10.3189/2012J0G11J020.

Wesche, C., Dierking, W., 2012. Iceberg signatures and detection in SAR images in two test regions of the Weddell Sea, Antarctica. J. Glaciol. 58, 325–339. https://doi.org/10.3189/2012J0G11J020.

Willis, C.J., Macklin, J.T., Partington, K.C., Teleki, K.A., Rees, W.G., Rees, W.G., 1996. Iceberg detection using ers-1 synthetic aperture radar. Int. J. Remote Sens. 17, 1777–1795. https://doi.org/10.1080/01431169608948739.

Wolken, G.J., et al., 2020. Glaciers and Ice Caps Outside Greenland. Arctic Report Card. https://arctic.noaa.gov/report-card/report-card-2020/glaciers-and-ice-caps-outside-greenland/.

Yackel, J.J., Barber, D.G., Papakyriakou, T.N., Breneman, C., 2007. First-Year Sea ice spring melt transitions in the Canadian Arctic archipelago from time-series synthetic aperture radar data, 1992–2002. Hydrol. Process. 21 https://doi.org/10.1002/hyp.

Zakharov, I., Power, D., Howell, M., Warren, S., 2017. Improved detection of icebergs in sea ice with RADARSAT-2 polarimetric data. In: Int. Geosci. Remote Sens. Symp. 2017-July, pp. 2294–2297. https://doi.org/10.1109/IGARSS.2017.8127448.